# Light-Induced Phase Separation with Finite Wavelength Selection in Photophobic Microalgae

Isabelle Eisenmann,[1] Alfredo L'Homme,[2] Aliénor Lahlou,[3,4] Sandrine Bujaldon,[5] Thomas Le Saux,[3] Benjamin Bailleul,[5] Nicolas Desprat,[1,*] and Raphaël Jeanneret[1,†]

[1]*Laboratoire de Physique de l'Ecole normale supérieure, ENS, Université PSL, CNRS, Sorbonne Université, Université Paris Cité, F-75005 Paris, France*

[2]*Institute for Biological and Medical Engineering, Schools of Engineering, Medicine and Biological Sciences, Pontificia Universidad Católica de Chile, Santiago, Chile*

[3]*PASTEUR, Department of Chemistry, Ecole Normale Supérieure, PSL University, Sorbonne University, CNRS, Paris, France*

[4]*Sony Computer Science Laboratories, Paris, France*

[5]*Laboratory of Chloroplast Biology and Light Sensing in Microalgae, Institut de Biologie Physico Chimique, CNRS, Sorbonne Université, Paris 75005, France*

(Received 18 September 2024; accepted 14 August 2025; published 1 October 2025)

As with many motile microalgae, the freshwater species *Chlamydomonas reinhardtii* can detect light sources and adapt its motile behavior in response. Here, we show that suspensions of photophobic cells can be unstable to density fluctuations, as a consequence of shading interactions mediated by light absorption. In a circular illumination geometry, this mechanism leads to the complete phase separation of the system into transient branching patterns, providing experimental evidence of finite wavelength selection through a motility-induced phase separation mechanism. The finite wavelength selection is a consequence of a vision-based interaction length scale which is fixed by the illumination geometry. A simple drift-diffusion framework allows us to understand how the wavelength depends on global cell density, light intensity, and medium viscosity. Finally, we show that this active phase separation shields individual cells from the deleterious effects of high light intensity, demonstrating that phototaxis can efficiently contribute to photoprotection through collective behaviors on short timescales.

DOI: 10.1103/ss2g-kbpj

The emergence of spatiotemporal structures is widespread in active matter systems. Examples include flocks of birds [1,2], bacterial turbulence [3], bioconvective instabilities [4], hydrodynamic and magnetic instabilities [5–9], Bose-Einstein-like condensation [10,11] or motility-induced phase separation (MIPS) [12,13]. Finite wavelength instabilities, where the system undergoes a selection of periodic patterns, have been described in different experimental systems: pearling and waving instabilities in jets of active particles [5–9], periodic arrays of horizontal plumes in magnetotactic bacteria [14], dendrites in gyrotactic microalgae experiencing photobioconvective instabilities [15], vortex arrays of sperm cells or microtubules from hydrodynamic or nematic alignment interactions [16,17], and fingering instabilities in microrollers with hydrodynamic interactions [18]. However, for populations of constant size, MIPS-type instabilities seem only to generate patterns ranging from one to many clusters randomly distributed in space [12,13,19–21].

Collections of microorganisms constitute an interesting playground for investigating self-organization from relatively simple interaction rules between the agents [22]. Here, we show that a dilute suspension of motile microalgae *Chlamydomonas reinhardtii* [23,24] undergoing negative phototaxis (i.e., fleeing light sources) can phase separate into a dense liquidlike phase with a selection of a finite wavelength from a MIPS-like scenario. In our experimental circular geometry, the patterns take the shape of branched trees, with regularly spaced filaments converging at the center of the system. This instability is triggered by the interplay between negative phototaxis and light absorption by the cells: algae hide behind each other when fleeing multiple light sources. Our simple model suggests that the selection of a finite wavelength emerges from the nonlocality of the shading interactions. Based on a drift-diffusion framework, this model captures experimental observations like critical cell density or light intensity and yields quantitative predictions of the wavelength of the instability. Finally, we establish that algae gathered in the

*Contact author: nicolas.desprat@phys.ens.fr

†Contact author: raphael.jeanneret@phys.ens.fr

*Published by the American Physical Society under the terms of the Creative Commons Attribution 4.0 International license. Further distribution of this work must maintain attribution to the author(s) and the published article's title, journal citation, and DOI.*

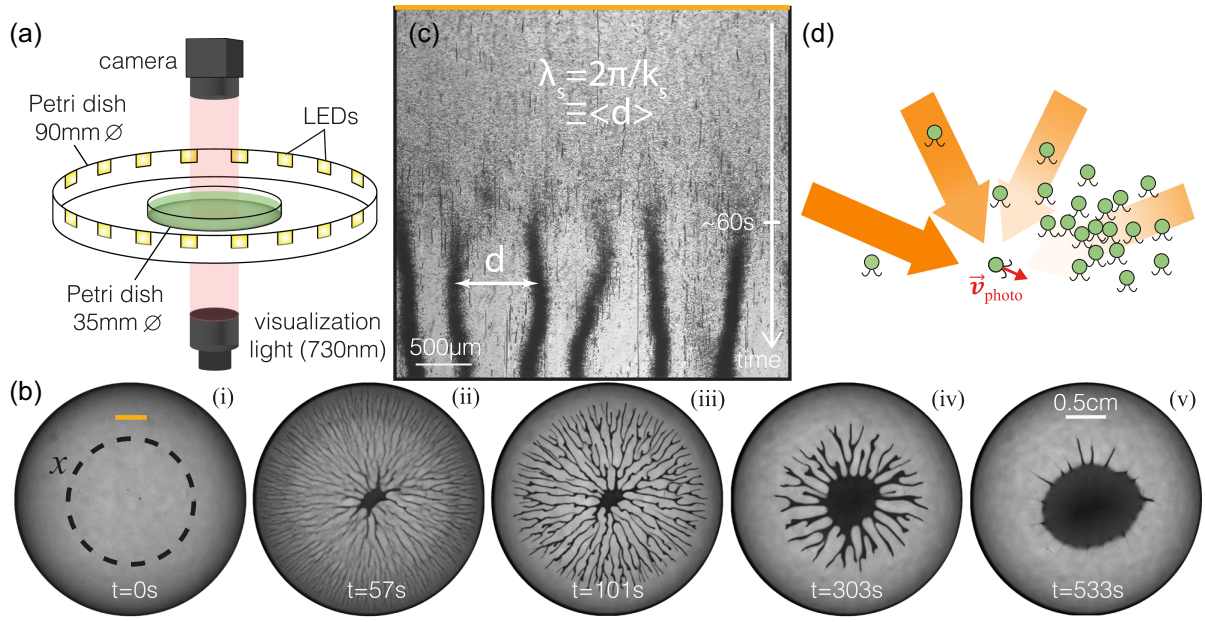



FIG. 1. A density instability from negative phototaxis and light absorption. (a) Schematics of the setup. A suspension of *Chlamydomonas reinhardtii* is loaded in a Petri dish, surrounded by a ring of LEDs. Visualization is done with a far-red collimated light. (b) Time lapse of the light-induced phase separation ($\rho_0 = 2.8 \times 10^6$ cells/ml). Initially, the suspension is homogeneous. After switching on the lights, cells start migrating toward the center. After 1 min, dense filaments appear everywhere. These then evolve into interconnected dense branches that retract slowly toward the center. Finally, a steady, dense "drop" is found in the center. $x$ is the azimuthal coordinate used in the model. (c) Kymograph of the destabilization process along the yellow line in (b)(i). The initial homogeneous suspension destabilizes into dense branches separated by a well-defined wavelength $\lambda_s$. (d) Schematics illustrating the mechanism of the instability. Because of light absorption, a stochastic density fluctuation creates an inhomogeneous light environment (orange arrows). Surrounding cells then flee from the most intense lights toward the fluctuation.

dense phase are collectively protected from the deleterious effects of light.

To characterize the photophobic response of populations of *C. reinhardtii* cells, we used a white light-emitting diode (LED) strip surrounding cells suspended in a liquid tris-acetate-phosphate (TAP) medium [23] and sitting in a cylindrical dish [see Fig. 1(a) and Appendixes A and B]. We monitored the suspension with a collimated far-red light (730 nm) that does not interfere with phototaxis. In our conditions cells only performed negative phototaxis in the range of light intensities that we used [25]. We homogenized the suspension and then switched on the LED lights [Fig. 1(i)], triggering individual cells to migrate toward the center of the dish. After After $\sim 30$ s denser areas started forming throughout the Petri dish (Movie S1 in the Supplemental Material) [25]. These denser areas then evolved into long and connected "branches" [Figs. 1 and 1]. After phase separation the emerging "liquid" phase was characterized by seemingly isotropic motion of the cells in its bulk (Movies S2 and S3 in the Supplemental Material) [25]. We estimated that the density of the dense phase was $\rho_{\mathrm{drop}} \approx 3 \times 10^9$ cells/ml (~50% volume fraction), 3 orders of magnitude larger than the initial cell concentration [25]. The average interbranch distance $\lambda_s \equiv \langle d \rangle$ [Fig. 1(c)] was independent of the radial position during early pattern retraction (see Appendix B and [25]) and will be used in the following to characterize the density instability. The final retraction of the pattern involved branches emptying in the vertices, leading to an increasing branch width and inter-branch distance with time (Movie S1 in the Supplemental Material [25]), until merging into a drop at the center of the system [Figs. 1 and 1(v)].

No cell-cell adhesion was involved in the density instability and phase separation, since the pattern immediately started to blur when the light sources were switched off (Movie S4 in the Supplemental Material [25]) due to the diffusive run-and-tumble motion of the algae in the dark [41]. Neither bioconvection nor gyrotaxis [4,15] were involved, since the pattern is confined within ~50–60 μm at the very bottom of the dish [25], which contrasts with the dendrite instability described in [15,42]. Hydrodynamic interactions between the aligned pullers cannot explain the instability either because of the repulsive nature of these interactions perpendicular to the swimming direction [25]. Chemical interactions (quorum sensing, chemotaxis, etc.) can also be excluded given the timescale for the emergence of the dense phase (typically ~1 min). Finally, the number of branches and their location were not correlated with the discreteness of the light sources as long as the inter-LED distance remained short enough [25].

Once formed, the branching pattern retracted slowly compared to the typical swimming speed of individual cells [25]. Looking at individual branches, we noticed that

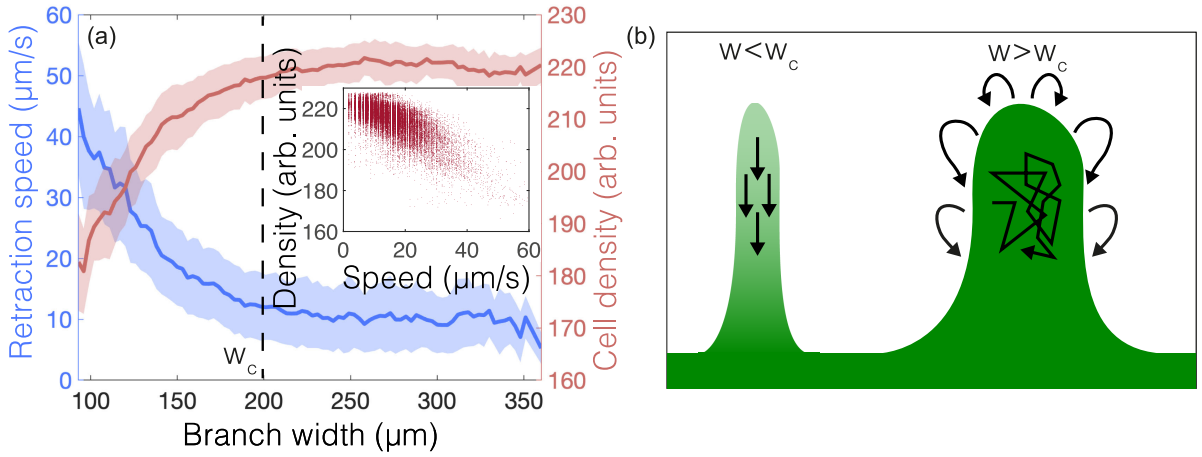



FIG. 2. Dynamics of branch retraction. (a) The retraction speed of individual branches decreases with branch width until reaching a plateau at ∼10 μm/s for $w > w_c \approx 200$ μm (blue curve). This evolution mirrors that of the branch density (red curve) which saturates above $w_c$. The shaded area shows 2 standard deviations. Inset: scatterplot of branch density versus retraction speed for all individual data points used to produce the main figure. (b) When branches are thin enough ($w < w_c$), light goes through and cells proceed fleeing the lights, resulting in a net phototactic flux in the bulk of the branches and thus high retraction speeds. When branches are too wide ($w > w_c$), light intensity within the bulk of the branch becomes too low for the cells to perform phototaxis. A downward flux is still present at the interface between the dense and dilute phases.

thin branches retracted much faster than wide ones (Movie S1 of the Supplemental Material [25]). On average the speed of tip retraction decreased with branch width until reaching a plateau for $w > w_c \sim 200$ μm [Fig. 2(a), blue curve]. Conversely, the average cell concentration in the branches increased with branch width until plateauing when the width exceeded $w_c$ [Fig. 2(a), red curve]. The anticorrelation between branch retraction speed and cell density [Fig. 2(a) inset] could be understood by considering light absorption by the cells. In the dense phase, the characteristic length scale for light absorption by cells was estimated to be $L_{\mathrm{abs}} \approx 10$ μm (Appendix C). When branches were a few tens of $L_{\mathrm{abs}}$ wide, the light intensity within branches became too low for cells to perform phototaxis, resulting in diffusive isotropic motion dominated by collisions [see Fig. 2(b) and Movie S3 of the Supplemental Material [25] ]. However, cells at the interface between the dense and dilute phases still sensed light and moved toward the center [see Movie S5 of the Supplemental Material [25] and Fig. 2(b)]. Such a mechanism led to a net retraction speed of the branches that was mostly independent of their width. If, on the contrary, branches were thin enough, light penetrated into the branch and all cells proceeded to flee the light source, resulting in a net phototactic flux in the bulk of the branches and thus higher net retraction speeds [see Fig. 2(b) and Movie S6 of the Supplemental Material [25] ].

Light absorption by branches in turn influenced the motion of cells in neighboring branches. As shown in Movie S7 of the Supplemental Material [25], thin branches could indeed be locally attracted by wider ones and flow into them.

Based on the above observations, we proposed a simple mechanism for explaining the initial destabilization and phase separation of the photophobic suspension. When the lights were turned on, cells reoriented and moved toward the center [Movie S2 of the Supplemental Material [25] ]. At this stage, cells mainly detected light coming from their side since the eyespot—the light detector located at the cell's equator—spins along the radial swimming direction [43–46]. Therefore, any spontaneous positive fluctuation of the local cell density along the azimuthal direction could induce a phototactic bias toward the denser region [see Fig. 1(d) and Movie S2 of the Supplemental Material [25] ]. The initial stochastic density fluctuation could therefore be amplified from bias in the motility mediated by shading interactions, leading to the destabilization of the suspension and the phase separation of the system in a MIPS-like scenario.

Following this proposed mechanism, we now describe a simple phenomenological model to account for the density instability and quantitatively compare it to our experimental results. We consider a one-dimensional (1D) description [25] of the cell density field $\rho(x,t)$ along the azimuthal direction $x$ [Fig. 1(i)]. We model the evolution of $\rho(x,t)$ with a drift-diffusion equation [25]

$$\frac{\partial \rho}{\partial t} = D\frac{\partial^2 \rho}{\partial x^2} - \frac{\partial \rho v_{\mathrm{photo}}}{\partial x} \tag{1}$$

$$v_{\mathrm{photo}}(x,t) = \alpha\left[\int_x^{x+\Delta x} \rho(x',t)dx' - \int_{x-\Delta x}^{x} \rho(x',t)dx'\right], \tag{2}$$

where the drift term $v_{\mathrm{photo}}$ describes the phototactic bias toward regions of higher densities. We assume that the cells

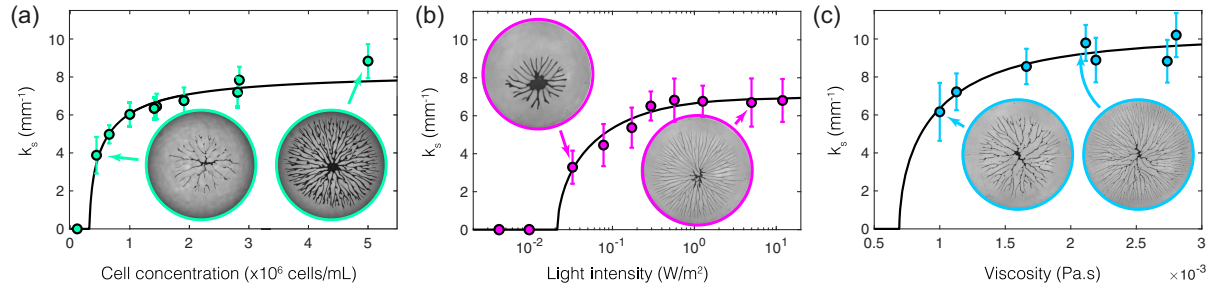



FIG. 3. Quantification of the density instability and comparison with the model. (a)–(c) Experimentally measured wave number of the instability $k_s$ as a function of the following control parameters. (a) Cell density. (b) Average light intensity per LED. (c) Medium viscosity. The error bars represent standard deviations of at least three replicas. The solid black lines correspond to the fitted analytical expression $k_s^{(\mathrm{th})}$ [Eq. (4)]. Insets: snapshots of the system at the times at which $k_s$ was evaluated.

are able to detect left-right asymmetries in cell density with a sensitivity $\alpha$ and an interaction distance $\Delta x$ associated with vision-based interactions [1,47–49]. Noise in the ability of cells to follow a specific direction is modeled through a constant diffusion $D$.

By performing a linear stability analysis of these equations (Appendix D), we showed that the homogeneous state $\rho(x,t)=\rho_0$ is unstable as soon as the parameter $\beta=\alpha\rho_0/D$ is larger than a critical value $\beta_c=1/\Delta x^2$. In such a case, the selected mode is predicted to be

$$k_s^{(\mathrm{th})}=\frac{1}{\Delta x}\,\mathrm{sinc}^{-1}_{[0;\pi]}\left(\frac{1}{\beta\Delta x^2}\right), \tag{3}$$

where $\mathrm{sinc}^{-1}_{[0;\pi]}(y)$ $(y\in[0,1])$ is the inverse function of the sine cardinal $\mathrm{sinc}(x)$, where $x\in[0,\pi]$. When $\beta$ becomes much larger than $\beta_c$, $k_s^{(\mathrm{th})}$ saturates at a value $k_{s,\max}^{(\mathrm{th})}=\pi/\Delta x$, which is set by the interaction length $\Delta x$. Indeed, density peaks developing closer than twice the interaction distance merge, leaving on average at least $2\Delta x$ space between density fluctuations.

This model can be compared to the wave number selected at the onset of pattern formation when different control parameters are varied, namely, the initial cell concentration $\rho_0$, the average light intensity $I_{\mathrm{LED}}$, and the viscosity of the medium $\eta$ [25]. The wave number is defined here as $k_s=2\pi/\lambda_s$, with $\lambda_s$ the average interbranch distance [see Fig. 1(a) and Appendix B]. The wave number $k_s$ increased as the experimental parameters were increased [see Figs. 3(a)–3(c) and Movies S8–S10 in the Supplemental Material [25] ]. When the cell density was fixed (i.e., when $I_{\mathrm{LED}}$ or $\eta$ is varied), this also implied that branches got thinner [see the insets of Figs. 3(b) and 3(c) and the Supplemental Material [25] ]. Moreover, the wave numbers saturated at a similar value $k_{s,\max}\sim 7-10$ mm$^{-1}$ (corresponding to a minimal average interbranch distance $\lambda_{s,\min}\sim 600$–$900$ μm). Finally, at low cell density ($\rho_0<0.3\times10^6$ cells/ml) or light intensity ($I_{\mathrm{LED}}<3\times10^{-2}$ W/m$^2$), the system did not destabilize along the azimuthal direction, but cells still accumulated at the center of the dish (Movies S8 and S9 of the Supplemental Material [25]).

To compare experiments with the model, we had to make hypotheses as to how the parameters $D$ and $\alpha$ (and therefore $\beta$) depend on our experimental parameters $\eta$ and $I_{\mathrm{LED}}$. The diffusion coefficient $D$ was taken to be the run-and-tumble diffusivity in the dark and therefore assumed to be written $D(\eta)=D_0\eta_0^2/\eta^2$ [25]. The phototactic sensitivity $\alpha$ was modeled by a Hill function $\alpha=aI_{\mathrm{LED}}^p/(K^p+I_{\mathrm{LED}}^p)$ (with $p=0.7$ and $K$ the light intensity at which the response is half the maximum) as previously reported for channelrhodopsins, the proteins that detect light [25,50–52]. Overall, this led to the following prediction for the experimental evolution of the selected mode $k_s$:

$$\begin{aligned}k_s&=k_s^{(\mathrm{th})}(\rho_0,\eta,I_{\mathrm{LED}})\\&=\frac{1}{\Delta x}\,\mathrm{sinc}^{-1}_{[0;\pi]}\left(\frac{D_0}{a\rho_0\Delta x^2}\frac{\eta_0^2}{\eta^2}\frac{K^p+I_{\mathrm{LED}}^p}{I_{\mathrm{LED}}^p}\right).\end{aligned} \tag{4}$$

This model reproduced our experimental observations [the black curves in Figs. 3(c)] and returned fitting parameters $\Delta x\approx 340$ μm and $a\approx 4\times10^{-13}$ m$^3$/s consistent between the three sets of independent experiments [25], demonstrating that our simple 1D approach captured the physics of the phenomenon. We drew the expected phase diagram of the system obtained from the mean values of the fitting parameters and compared it to the experimental points [Figs. 4(a) and 4(b)]. The interaction length $\Delta x$ extracted from the fit to the model was about 40 times the size of an alga, resulting therefore in highly nonlocal interactions. We noticed that an interaction length of 340 μm was compatible with the size of the shadows $\Delta x_{\mathrm{geo}}$ created by the branches in our illumination geometry [25]. Changing the illumination angle $\gamma$ [25] should therefore modify the selected wave number. We tested this hypothesis by changing the height of the LED ring between $H_{\mathrm{LED}}\approx$ 5.5 and 12.5 mm at fixed cell concentration, light intensity, and medium viscosity and obtained wave numbers $k_s$

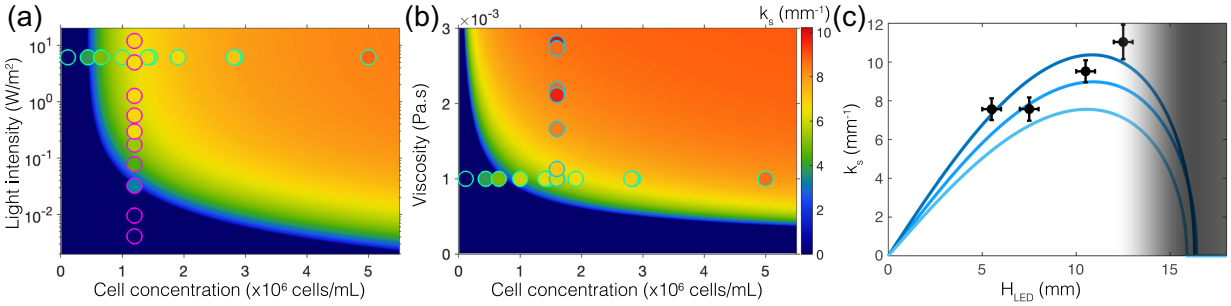



FIG. 4. Model predictions. (a),(b) Predicted phase diagram of the system where, for each set of variables $(\rho_0, I_{\mathrm{LED}})$ and $(\rho_0, \eta)$, we take the average value of the fitting parameters $a$ and $\Delta x$. (c) Experimentally measured wave number of the instability $k_s$ as a function of the height of the LED ring in the setup $H_{\mathrm{LED}}$. The blue curves are theoretical predictions based on the expression of $k_s^{(\mathrm{th})}$ with $\Delta x = \Delta x_{\mathrm{geo}}(H_{\mathrm{LED}})$ using the previously measured average values of the parameters (blue, mean; dark and light blue, standard).

consistent with our model when considering $\Delta x = \Delta x_{\mathrm{geo}}(H_{\mathrm{LED}})$ without fitting parameters [see Fig. 4(c) and Movie S13 in the Supplemental Material [25] ].

Between the initial dilute and homogeneous state and the emerging dense phase, the characteristic length scale for light absorption decreased from a few centimeters to a couple of cells widths. We then wondered whether the crowded environment of the dense phase could be beneficial for the algae with regard to the harmful effects of excess light on the photosynthetic machinery, i.e., photoinactivation of photosystem II (PSII). Photoinactivation is measured by the ratio $F_v/F_m$ through chlorophyll fluorescence measurements [53]. Our results (see Fig. 5, Appendix E, and Sec. S15 in the Supplemental Material [25]) showed that the decrease of the ratio $F_v/F_m$ was much smaller in the presence of branching patterns than when cells were continuously stirred (Fig. 5, solid lines). We also showed that the decrease of $F_v/F_m$ was amplified when the repair of damaged PSII was prevented by the chloroplast translation inhibitor lincomycin (Fig. 5, dashed lines). This indicated that the emergent light-induced phase separation of the suspension provided a collective function to the cell population by effectively protecting it from the harmful lights. Such collective protection, reminiscent of chloroplast reorganization in plants [54], builds up quickly (approximately a minute) and therefore complements well other individual photoprotective mechanisms that require longer light exposure (roughly minutes to hours) for synthesizing effector proteins [55].

In our system, suspensions of photophobic microalgae destabilize and phase separate into ordered branching patterns characterized by a finite wavelength. We have shown that phase separation is the consequence of biased motility toward regions of higher cell density, mediated by shading interactions, giving rise to a MIPS-like scenario. We have demonstrated that the dense phase is akin to a liquid phase, with cell motion still taking place and being isotropic, dominated by collisions. Our phenomenological model demonstrates that the nonlocality of the shading interactions between the cells is essential to quantitatively explain the selected patterns. This shows that nonlocality is an important feature of tactic interactions that could play a role in other experimental situations. In addition, the quantification of the intensity fields using a recently developed fluorescence technique [25,56] suggests that in our setup, cells do not follow the light intensity gradients, as had been found in other experimental situations [15,57]. Such observations raise questions regarding the way these cells actually use light as a guide to navigate, particularly when facing multiple light sources. Our understanding of phototaxis would therefore gain in having dedicated experiments to better link microscopic swimming properties to coarse-grained continuum equations at the population level. Finally, the phenomenon at play, which leads to the formation of a dense phase with a large volume fraction of ~50%, could benefit the microalgal industry in order to preconcentrate the biomass before harvesting, which currently represents a real bottleneck in the use of these organisms for clean energy, drugs, or food production [58,59].

*Acknowledgments*—R. J., N. D., and I. E. warmly thank Julien Tailleur for the insightful discussion on active phase separation, for suggesting a change in height of the LED ring, and for the critical reading of the manuscript. I. E. thanks Michael Shelley for the interesting discussions on the mapping of the model with the porous medium equation. R. J. thanks Adrien Izzet and Annie Colin for the use of their rheometer. The work of R. J. was supported by the Junior Research Chair Programme (Grants No. ANR-10-LABX-0010 and No. ANR-10-IDEX-0001-02 PSL), and that of I. E. was supported by an ED-PIF doctoral fellowship.

[1] M. Ballerini *et al.*, Interaction ruling animal collective behavior depends on topological rather than metric distance: Evidence from a field study, Proc. Natl. Acad. Sci. U.S.A. **105**, 1232 (2008).

[2] A. Cavagna, Al. Cimarelli, I. Giardina, G. Parisi, R. Santagati, F. Stefanini, and M. Viale, Scale-free correlations in starling flocks, Proc. Natl. Acad. Sci. U.S.A. **107**, 11865 (2010).
[3] C. Dombrowski, L. Cisneros, S. Chatkaew, R. E. Goldstein, and J. O. Kessler, Self-concentration and large-scale coherence in bacterial dynamics, Phys. Rev. Lett. **93**, 098103 (2004).
[4] M. A. Bees, Advances in bioconvection, Annu. Rev. Fluid Mech. **52**, 449 (2020).
[5] L. Jibuti, L. Qi, C. Misbah, W. Zimmermann, S. Rafaï, and P. Peyla, Self-focusing and jet instability of a microswimmer suspension, Phys. Rev. E **90**, 063019 (2014).
[6] T. Ishikawa, T.-N. Dang, and E. Lauga, Instability of an active fluid jet, Phys. Rev. Fluids **7**, 093102 (2022).
[7] N. Waisbord, C. Lefèvre, L. Bocquet, C. Ybert, and C. Cottin-Bizonne, Destabilization of a flow focused suspension of magnetotactic bacteria, Phys. Rev. Fluids **1**, 053203 (2016).
[8] F. Meng, D. Matsunaga, and R. Golestanian, Clustering of magnetic swimmers in a Poiseuille flow, Phys. Rev. Lett. **120**, 188101 (2018).
[9] G. Junot, M. De Corato, and P. Tierno, Large scale zigzag pattern emerging from circulating active shakers, Phys. Rev. Lett. **131**, 068301 (2023).
[10] R. Golestanian, Bose-Einstein-like condensation in scalar active matter with diffusivity edge, Phys. Rev. E **100**, 010601(R) (2019).
[11] F. Meng, D. Matsunaga, B. Mahault, and R. Golestanian, Magnetic microswimmers exhibit Bose-Einstein-like condensation, Phys. Rev. Lett. **126**, 078001 (2021).
[12] M. E. Cates and J. Tailleur, Motility-induced phase separation, Annu. Rev. Condens. Matter Phys. **6**, 219 (2015).
[13] J. O'Byrne, A. Solon, J. Tailleur, and Y. Zhao, An introduction to motility-induced phase separation, in *Out-of-Equilibrium Soft Matter*, edited by C. Kurzthaler, L. Gentile, and H. A. Stone (Royal Society of Chemistry, London, 2023).
[14] A. Théry, L. Le Nagard, J.-C. Ono-dit-Biot, C. Fradin, K. Dalnoki-Veress, and E. Lauga, Self-organisation and convection of confined magnetotactic bacteria, Sci. Rep. **10**, 13578 (2020).
[15] A. Ramamonjy, J. Dervaux, and P. Brunet, Nonlinear phototaxis and instabilities in suspensions of light-seeking algae, Phys. Rev. Lett. **128**, 258101 (2022).
[16] I. H. Riedel, K. Kruse, and J. Howard, A self-organized vortex array of hydrodynamically entrained sperm cells, Science **309**, 300 (2005).
[17] Y. Sumino, K. H. Nagai, Y. Shitaka, D. Tanaka, K. Yoshikawa, H. Chaté, and K. Oiwa, Large-scale vortex lattice emerging from collectively moving microtubules, Nature (London) **483**, 448 (2012).
[18] M. Driscoll *et al.*, Unstable fronts and stable "critters" formed by microrollers, Nat. Phys. **13**, 375 (2016).
[19] R. Matas-Navarro, R. Golestanian, T. B. Liverpool, and S. M. Fielding, Hydrodynamic suppression of phase separation in active suspensions, Phys. Rev. E **90**, 032304 (2014).
[20] H. Zhao, A. Košmrlj, and S. S. Datta, Chemotactic motility-induced phase separation, Phys. Rev. Lett. **131**, 118301 (2023).
[21] M. N. Van Der Linden, L. C. Alexander, D. G. Aarts, and O. Dauchot, Interrupted motility induced phase separation in aligning active colloids, Phys. Rev. Lett. **123**, 098001 (2019).
[22] E. Ben-Jacob, I. Cohen, and H. Levine, Cooperative self-organization of microorganisms, Adv. Phys. **49**, 395 (2000).
[23] E. S. Harris, *The Chlamydomonas Sourcebook* (Elsevier, New York, 2009).
[24] R. Jeanneret, M. Contino, and M. Polin, A brief introduction to the model microswimmer Chlamydomonas reinhardtii, Eur. Phys. J. Special Topics **225**, 2141 (2016).
[25] See Supplemental Material at http://link.aps.org/supplemental/10.1103/ss2g-kbpj, which includes Refs. [26–40], for complementary descriptions of the experiments, full development of the model, and supplementary movies.
[26] T. De Mooij, G. De Vries, C. Latsos, R. H. Wijffels, and M. Janssen, Impact of light color on photobioreactor productivity, Algal Res. **15**, 32 (2016).
[27] D. S. Bright and E. B. Steel, Two-dimensional top hat filter for extracting spots and spheres from digital images, J. Microsc. **146**, 191 (1987).
[28] L. Vincent and P. Soille, Watersheds in digital spaces: An efficient algorithm based on immersion simulations, IEEE Trans. Pattern Anal. Mach. Intell. **13**, 583 (1991).
[29] T. Ishikawa and T. J. Pedley, Coherent structures in monolayers of swimming particles, Phys. Rev. Lett. **100**, 088103 (2008).
[30] K. Drescher, R. E. Goldstein, N. Michel, M. Polin, and I. Tuval, Direct measurement of the flow field around swimming microorganisms, Phys. Rev. Lett. **105**, 168101 (2010).
[31] A. Giometto, F. Altermatt, A. Maritan, R. Stocker, and A. Rinaldo, Generalized receptor law governs phototaxis in the phytoplankton Euglena gracilis, Proc. Natl. Acad. Sci. U.S.A. **112**, 7045 (2015).
[32] Y. Leroyer and A. Würger, Drift-diffusion kinetics of a confined colloid, J. Phys. Condens. Matter **22**, 195104 (2010).
[33] K. Anguige and C. Schmeiser, A one-dimensional model of cell diffusion and aggregation, incorporating volume filling and cell-to-cell adhesion, J. Math. Biol. **58**, 395 (2009).
[34] N. J. Armstrong, K. J. Painter, and J. A. Sherratt, A continuum approach to modelling cell-cell adhesion, J. Theor. Biol. **243**, 98 (2006).
[35] S. Coppola and V. Kantsler, Green algae scatter off sharp viscosity gradients, Sci. Rep. **11**, 399 (2021).
[36] M. R. Stehnach, N. Waisbord, D. M. Walkama, and J. S. Guasto, Viscophobic turning dictates microalgae transport in viscosity gradients, Nat. Phys. **17**, 926 (2021).
[37] N. Murata, S. Takahashi, Y. Nishiyama, and S. I. Allakhverdiev, Photoinhibition of photosystem II under environmental stress, Biochim. Biophys. Acta Bioenerg. **1767**, 414 (2007).
[38] S. Takahashi and N. Murata, How do environmental stresses accelerate photoinhibition?, Trends Plant Sci. **13**, 178 (2008).
[39] R. Uhl and P. Hegemann, Adaptation of Chlamydomonas phototaxis: I. A light-scattering apparatus for measuring the

phototactic rate of microorganisms with high time resolution, Cell Motil. Cytoskeleton **15**, 230 (1990).
[40] T. Takahashi and M. Watanabe, Photosynthesis modulates the sign of phototaxis of wild-type Chlamydomonas reinhardtii: Effects of red background illumination and 3-(3',4'-dichlorophenyl)-1,1-dimethylurea, FEBS Lett. **336**, 516 (1993).
[41] M. Polin, I. Tuval, K. Drescher, J. P. Gollub, and R. E. Goldstein, Chlamydomonas swims with two "gears" in a eukaryotic version of run-and-tumble locomotion, Science **325**, 487 (2009).
[42] A. Ramamonjy, P. Brunet, and J. Dervaux, Pattern formation in photo-controlled bioconvection, J. Fluid Mech. **971**, A29 (2023).
[43] K. W. Foster and R. D. Smyth, Light antennas in phototactic algae, Microbiol. Rev. **44**, 572 (1980).
[44] K. Schaller, R. David, and R. Uhl, How Chlamydomonas keeps track of the light once it has reached the right phototactic orientation, Biophys. J. **73**, 1562 (1997).
[45] R. R. Bennett and R. Golestanian, A steering mechanism for phototaxis in Chlamydomonas, J. R. Soc. Interface **12**, 20141164 (2015).
[46] K. C. Leptos, M. Chioccioli, S. Furlan, A. I. Pesci, and R. E. Goldstein, Phototaxis of Chlamydomonas arises from a tuned adaptive photoresponse shared with multicellular Volvocine green algae, Phys. Rev. E **107**, 014404 (2023).
[47] J. A. Cohen and R. Golestanian, Emergent cometlike swarming of optically driven thermally active colloids, Phys. Rev. Lett. **112**, 068302 (2014).
[48] F. Ginelli, F. Peruani, M.-H. Pillot, H. Chaté, G. Theraulaz, and R. Bon, Intermittent collective dynamics emerge from conflicting imperatives in sheep herds, Proc. Natl. Acad. Sci. U.S.A. **112**, 12729 (2015).
[49] A. Filella, F. Nadal, C. Sire, E. Kanso, and C. Eloy, Model of collective fish behavior with hydrodynamic interactions, Phys. Rev. Lett. **120**, 35 (2018).
[50] H. Hartz, C. Nonnengässer, and P. Hegemann, The photoreceptor current of the green alga Chlamydomonas, Phil. Trans. R. Soc. B **338**, 39 (1992).
[51] N. J. G. Rorsman, C. M. Ta, H. Garnett, P. Swietach, and P. Tammaro, Defining the ionic mechanisms of optogenetic control of vascular tone by channelrhodopsin-2: Channelrhodopsin-2 in vascular optogenetics, Br. J. Pharmacol. **175**, 2028 (2018).
[52] H. Wang *et al.*, High-speed mapping of synaptic connectivity using photostimulation in channelrhodopsin-2 transgenic mice, Proc. Natl. Acad. Sci. U.S.A. **104**, 8143 (2007).
[53] N. R. Baker, Chlorophyll fluorescence: A probe of photosynthesis in vivo, Annu. Rev. Plant Biol. **59**, 89 (2008).
[54] N. Schramma, C. Perugachi Israëls, and M. Jalaal, Chloroplasts in plant cells show active glassy behavior under low-light conditions, Proc. Natl. Acad. Sci. U.S.A. **120**, e2216497120 (2023).
[55] E. Erickson, S. Wakao, and K. K. Niyogi, Light stress and photoprotection in Chlamydomonas reinhardtii, Plant J. **82**, 449 (2015).
[56] A. Lahlou *et al.*, Fluorescence to measure light intensity, Nat. Methods **20**, 1930 (2023).
[57] J. Arrieta, A. Barreira, M. Chioccioli, M. Polin, and I. Tuval, Phototaxis beyond turning: Persistent accumulation and response acclimation of the microalga Chlamydomonas reinhardtii, Sci. Rep. **7**, 3447 (2017).
[58] A. K. Koyande *et al.*, Microalgae: A potential alternative to health supplementation for humans, Food Sci. Hum. Wellness **8**, 16 (2019).
[59] G. Ferreira Mota *et al.*, Biodiesel production from microalgae using lipase-based catalysts: Current challenges and prospects, Algal Res. **62**, 102616 (2022).
[60] S. Strogatz, *Nonlinear Dynamics and Chaos: With Applications to Physics, Biology, Chemistry, and Engineering* (CRC Press, Boca Raton, 2018).
[61] N. Berne, T. Fabryova, B. Istaz, P. Cardol, and B. Bailleul, The peculiar NPQ regulation in the stramenopile Phaeomonas sp. challenges the xanthophyll cycle dogma, Biochim. Biophys. Acta, Bioenerg. **1859**, 491 (2018).

## End Matter

*Appendix A: Cell strain and culture*—A wild-type CC125 strain and eye-deficient mutant CC1101 were obtained from the Chlamydomonas Resource Center. Cells were grown in TAP [23] at $\sim 70\ \mu\mathrm{mol/m^2/s}$ and 25 °C on an orbital shaker at 140 rpm. Cells were synchronized by growing them in day-night illumination cycles (16 and 8 h, respectively). Cells were harvested in the exponential phase (concentration between $\sim 0.1$ and $\sim 5 \times 10^6$ cells/ml) and placed for 20 min in the dark with aeration (in the open Petri dish used for the experiments, Falcon 353001, diameter 35 mm) before the experiments were conducted.

*Appendix B: Setup, visualization and image analysis*—Light sources were flexible white LED stripes (16 individual LEDs spaced 16.7 mm apart, RS Pro 153-3644) glued on the inner edge of a 90 mm diameter Petri dish. See the Supplemental Material [25] for a characterization of the light sources. The light intensity $I_{\mathrm{LED}}$ defined in the manuscript corresponds to the spatially averaged light intensity per LED as defined in the Supplemental Material [25]. Cells only performed negative phototaxis in the light intensity range we used ($I_{\mathrm{LED}} \geq 4\ \mathrm{mW/m^2}$). We visualized the small Petri dish containing the cell suspension using a collimated red light (Thorlabs M730L5 730 nm) that did not interfere with phototaxis and a CMOS camera (IDS, UI-3370CP-M-GL) mounted with an objective Tamron (ref. 002649).

To measure the branch wave number at the onset of instability, we first binarized the images by performing two kinds of thresholding [25]. The first was an Otsu thresholding using the same threshold for the entire image (with the threshold computed automatically from the histogram), which allows the central blob and large branches to be extracted. However, this type of thresholding misses small branches (the ones brighter than the central blob). Therefore, to also extract small branches, we also applied an adaptive thresholding where the threshold was computed automatically on small windows with a width of 31 pixels (∼500 μm) browsing the image. The final binary image is then the sum of the two thresholdings [Figs. S2(a) and S2(b) of the Supplemental Material [25] ]. The masks were then skeletonized using the Lee method implemented in PYTHON SCIKIT library. We then counted the number of branches along concentric circles and divided by the perimeter to obtain the branch density $1/\lambda_s$ and the wave number $k_s = 2\pi/\lambda_s$ (following the notation of the manuscript). We measured and averaged the wave number over a 7.5 s duration [the pink shading in Fig. S2(c) of the Supplemental Material [25] ], 15 s after the peak in Fig. S2(c) in the Supplemental Material [25] [corresponding to the appearance of a not fully defined pattern; see Fig. S2(a)(i) of the Supplemental Material [25] ]. Because the branch density is more or less invariant along radii far enough from the center and the edge of the pattern [Fig. S2(d) of the Supplemental Material [25] ], we averaged the wave number over a ring between 50% and 90% of the total radial length of the pattern [the shaded blue areas in Figs. S2(b) and S2(d) of the Supplemental Material [25] ].

The proxy for the cell density in the branches [Fig. 2(a)] was simply the inverted gray level of our 8 bit images. The retraction speed of the branches was computed over a time interval of 10 s. The plots in Fig. 2(a) were obtained by discretizing the branch widths into bins 3 μm wide and collecting data from four different replicas at the cell concentration $2.8 \times 10^6$ cells/ml.

*Appendix C: Measurement of absorption coefficient and characteristic length scale of light propagation*—To estimate the characteristic length scale of light propagation in the dense phase, we first measured the absorption coefficient per unit length and the cell density of the cell suspension (in the dilute limit) via classical optical density measurements (using a Biospectrometer Basic from Eppendorf). We measured the absorbance $A = \log(I_0/I_T)$ at 460 nm (corresponding to the peak sensitivity of the channelrhodopsin molecules of the eyespot) in a cuvette with a length of $L_{\mathrm{cuv}} = 1$ cm at different cell concentrations $\rho_0$ between ∼0.3 and $6 \times 10^6$ cells/ml and obtained a linear relationship consistent with a simple Beer-Lambert law for light absorption by the cells (Fig. S10 of the Supplemental Material [25]), $A = \log(I_0/I_T) = \kappa_\rho \rho_0 L_{\mathrm{cuv}}$, with $\kappa_\rho$ the absorption coefficient per unit length and cell density of the cell suspension. Fitting the experimental absorbance curve returned $\kappa\rho = 3 \times 10^{-7}$ cm$^2$.

From this measurement we extrapolated to the high cell density regime in order to extract a characteristic length scale for light propagation in the dense phase, $L_{\mathrm{abs}} = 1/\kappa_\rho \rho_{\mathrm{drop}} \approx 10$ μm. This length corresponds to the width of approximately two cells, showing that a single cell already absorbs a significant quantity of light.

*Appendix D: Linear stability analysis of the model and mode selection*—Injecting solutions of the type $\tilde{\rho}(\tilde{x},\tilde{t}) = 1 + \epsilon e^{\tilde{\sigma}\tilde{t}} e^{-i\tilde{k}\tilde{x}} (\epsilon \ll 1)$ into the nondimensional version of Eq. (1) [25] and keeping only terms of order $\epsilon$ [60], $\partial\tilde{\rho}/\partial\tilde{t} = \epsilon\tilde{\sigma} e^{\tilde{\sigma}\tilde{t}} e^{-i\tilde{k}\tilde{x}}$, $\partial^2\tilde{\rho}/\partial\tilde{x}^2 = -\epsilon\tilde{k}^2 e^{\tilde{\sigma}\tilde{t}} e^{-i\tilde{k}\tilde{x}}$, $\tilde{\rho}(\partial\tilde{q}/\partial\tilde{x}) = 2\epsilon[\cos(\tilde{k}\Delta\tilde{x}) - 1] e^{\tilde{\sigma}\tilde{t}} e^{-i\tilde{k}\tilde{x}} + O(\epsilon^2)$, and $\tilde{q}(\partial\tilde{\rho}/\partial\tilde{x}) = O(\epsilon^2)$, the dispersion relation is directly obtained (simplifying all $\epsilon$, $e^{\tilde{\sigma}\tilde{t}}$, and $e^{-i\tilde{k}\tilde{x}}$) as

$$\tilde{\sigma} = 2\tilde{\beta}(1 - \cos(\tilde{k}\Delta\tilde{x})) - \tilde{k}^2, \tag{D1}$$

which expresses the growth rate of the instability $\tilde{\sigma}$ for the spatial mode $\tilde{k}$. Returning to dimensional variables, we get

$$\frac{\sigma}{D\beta} = 2(1 - \cos(k\Delta x)) - \frac{k^2}{\beta} \tag{D2}$$

$$= f(k) - g(k), \tag{D3}$$

where $\beta = \alpha\rho_0/D$ and $f$ and $g$ are positive functions of $k$. The system is linearly unstable if and only if there exists a range of wave number $k$ for which the growth rate $\sigma$ is positive, i.e., $f(k) > g(k)$. By expanding the function $f$ to second order in $k$ ($f \sim 2[1 - (1 - k^2\Delta x^2/2)] \sim \Delta x^2 k^2$), we directly see that this is the case when $\Delta x^2 > 1/\beta$, i.e., $\beta > \beta_c = 1/\Delta x^2$. When $\beta \le \beta_c = 1/\Delta x^2, f(k) \le g(k)$ for all $k$ (Fig. S11 of the Supplemental Material [25], cyan and light blue curves), the growth rate $\sigma$ is always negative and the system is linearly stable. This situation is met experimentally when cell concentration or LED intensity is low [see Figs. 3(a) and 3(b) and Movies S8 and S9 of the Supplemental Material [25] ] or when using the eyespot mutant (Movie S11 of the Supplemental Material [25]), where cells migrated toward the center but did not develop branches. When $\beta$ increases above $\beta_c, f(k) > g(k)$ for some range of $k$ (Fig. S11 of the Supplemental Material, dark blue and pink curves [25]) and the system becomes unstable

(within the shaded areas of Fig. S11 of the Supplemental Material [25]).

In the latter case ($\beta > \beta_c$), the selected mode $k_s$ corresponds to the mode with the highest growth rate, i.e., the mode that maximizes $\sigma$ (the most unstable). By taking the derivative of $\sigma$ with $k$, we can show that the locations of the extrema of $\sigma$, $k_e$, are given by the relation $\mathrm{sinc}(k_e\Delta x) = 1/\beta\Delta x^2$, from which we can extract the global maximum [Eq. (3)]. The most unstable mode is a monotonically increasing function of $\beta$. When $\beta$ is much larger than $1/\Delta x^2 = \beta_c$, $k_s^{(\mathrm{th})}$ tends to a finite value simply given by $k_{s,\max}^{(\mathrm{th})} = \pi/\Delta x$.

*Appendix E: Measurement of chlorophyll fluorescence ratio*—High-light treatment was achieved via 30 min of illumination in the setup [Fig. 1(a)], with a 460 nm blue LED stripe at 78 $\mathrm{W/m^2} = 303$ $\mu\mathrm{mol/(m^2.s)}$ (JKL Components ZFS-85000HD-B). Cells quickly phase separated into a dense phase which remained stable during the entire high-light treatment. A shaken suspension (100 rpm) that cannot phase separate was submitted to the same light conditions to compare the evolution of the fluorescence ratio $F_v/F_m$, which was followed using a fluorescence CCD camera recorder (SpeedZen, JBeamBio, France) present in the laboratory of S. B. and B. B. at the Institut de Biologie Physico-Chimique [61]. A dark condition was also set as a control. During low light relaxation, cells were stirred at 140 rpm under low intensity white illumination [~8 $\mu\mathrm{mol/(m^2.s)}$]. The evolution of the ratio $F_v/F_m$ was followed by sampling directly from the Petri dishes along the course of the experiment. For assessing cells in the dense phase 5 µl was pipetted directly in the branches or the drop and diluted into 65 µL of centrifuged medium culture, while 70 µL was directly pipetted in the dilute conditions. More details on these experiments are given in Sec. S15 of the Supplemental Material [25].

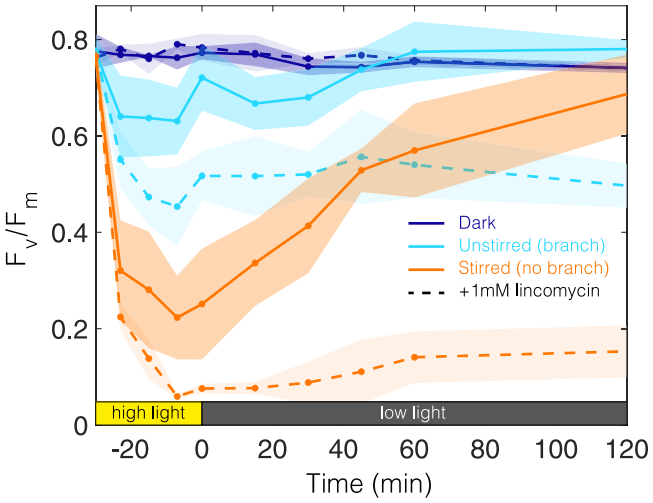



FIG. 5. Quantification of photoinhibition. Cells were exposed to 30 min of blue light, either letting cells phase separate (light blue curves) or preventing them from forming a dense phase by gently shaking the setup on an orbital shaker (orange curves). A control was kept in the dark (dark blue curves). Both conditions lead to the relaxation of $F_v/F_m$ to its initial value in the next 2 h at low light (solid lines). Adding the chloroplast inhibitor lincomycin prevents such relaxation (dashed lines), confirming that the drop in $F_v/F_m$ is indeed induced by the high-light treatment. Shaded areas correspond to 1 standard deviation of three biological replicas.

*Appendix F: Microscope movies*—Microscopy movies were done on inverted Olympus microscopes (IX73 or IX83) with a camera IDS UI-3000SE-M-GL or Hamamatsu Orca Fusion BT C15440-20UP and a 4 times magnification objective. A 780 nm long-pass filter (Thorlabs FGL780S) was placed on the light path to prevent phototactic stimulation of the cells by the visualization light.

*Appendix G: Viscosity experiments*—The viscosity of the medium was adjusted by adding methylcellulose (M0387, Sigma Aldrich, 1500cP) to TAP. See the Supplemental Material [25] for more details.